



HAL
open science

Thermodynamic model for lattice point defect-mediated semi-coherent precipitation in alloys

Maylise Nastar, Lisa Belkacemi, Estelle Meslin, Marie Loyer-Prost

► **To cite this version:**

Maylise Nastar, Lisa Belkacemi, Estelle Meslin, Marie Loyer-Prost. Thermodynamic model for lattice point defect-mediated semi-coherent precipitation in alloys. *Communications Materials*, 2021, 2, pp.32. 10.1038/s43246-021-00136-z . cea-03467616

HAL Id: cea-03467616

<https://cea.hal.science/cea-03467616>

Submitted on 6 Dec 2021

HAL is a multi-disciplinary open access archive for the deposit and dissemination of scientific research documents, whether they are published or not. The documents may come from teaching and research institutions in France or abroad, or from public or private research centers.

L'archive ouverte pluridisciplinaire **HAL**, est destinée au dépôt et à la diffusion de documents scientifiques de niveau recherche, publiés ou non, émanant des établissements d'enseignement et de recherche français ou étrangers, des laboratoires publics ou privés.



Distributed under a Creative Commons Attribution 4.0 International License

Thermodynamic model for lattice point defect-mediated semi-coherent precipitation in alloys

Maylise Nastar ¹, Lisa T. Belkacemi ¹, Estelle Meslin¹ & Marie Loyer-Prost¹

The formation of precipitates with an atomic volume different from their parent phase eventually leads to a loss of the lattice continuity at the matrix-precipitate interface. Here, we show the creation or removal of lattice sites mediated by lattice point defects is an accommodation mechanism of the coherency loss and even a precipitation driving force. We introduce a thermodynamic approach that rationalizes the selection of phases resulting from chemical and crystallographic constraints in relation to point defect properties. The resulting semi-coherent phase diagram and the precipitation kinetic model depend on the equilibrium phase diagram, the eigenstrain of the precipitating phase, and the chemical potential of point defects. From a joint experimental and modeling study, we uncover the prominent role of excess point defects in unforeseen phase transformations of the Fe-Ni metallic system under irradiation. By addressing the fundamental role of lattice point defects in the accommodation mechanisms of precipitation, we provide a step towards the understanding of semi-coherent phase transformations occurring in solid materials upon synthesis and in use.

¹Université Paris-Saclay, CEA, Service de Recherches de Métallurgie Physique, Gif-sur-Yvette, France. ✉email: mnastar@cea.fr

Secondary phase precipitates contribute to the microstructure of a material. In presence of precipitates, a material never really reaches its equilibrium state. It evolves by getting around or overcoming energy barriers it encounters on its way to equilibrium. Energy barriers can be related to the nucleation of finite-size secondary phases, resulting from the balance between the volume precipitation driving force and the energetic cost of forming a nuclei/matrix interface. The system activates accommodation mechanisms that reduce the nucleation barrier by decreasing the interface energy. Such mechanisms usually decrease the bulk precipitation driving force. A well-known example is the generation of an elastic strain preserving the lattice continuity between the precipitating phase and the parent phase along with specific directions. When precipitates have a small eigenstrain (stress-free strain) and the same crystallographic structure as the parent one, an elastic strain accommodation mechanism may lead to fully coherent precipitate/matrix interfaces. As outlined in Fig. 1a, b, the obtained two-phase equilibrium domain is reduced by the constraint of coherency^{1,2}.

Whenever the precipitate eigenstrain is not compensated by an elastic strain, precipitates feature a loss of coherency at the interface, i.e., the number of lattice sites across the interface is not conserved. It occurs through sequences of kinetic mechanisms involving lattice point and dislocation defects, such as the absorption of point defects condensing in precipitates and

forming extra atomic planes (dislocations)^{3,4} (Fig. 1c). In Al–Cu, the nucleation of the incoherent θ' phase on the coherent θ'' precipitates occurs through the injection of vacancies into θ'' ⁵ (as in Fig. 1d). In these examples, dislocations and point defects act as local sources and sinks of lattice sites. Thanks to their non-conservative nature, point defects may appear, transform, or annihilate. Although a thermodynamic formulation including defects is lacking, experimental observations clearly show that the selection of precipitating phases and their evolution is governed by the interplay between the chemistry of phases, interface constraints^{6,7}, diffusion properties^{8–10}, and lattice defects^{5,11}. Vacancy as a thermodynamic protagonist has been invoked to explain phase transformations of irradiated systems^{12,13}. Surprisingly, no one has ever considered the thermodynamic potential of the self-interstitial atom (SIA). In systems submitted to thermal quenching, severe mechanical solicitation, or irradiation, point defects are in excess. The removal of these point defects resulting from semi-coherent precipitation stabilizes the system, therefore increases the precipitation driving force^{12,14}.

By introducing the concept of a semi-coherent phase diagram, we challenge the standard formulation of the phase diagram. We add to the fundamental Gibbs free energy of solid phases, an energy term modeling the interplay between point defects and the volume constraints of a finite-size precipitate. Either as a precipitation driving force (in case of an excess of point defects) or as an accommodation mechanism (in thermal conditions), the effect

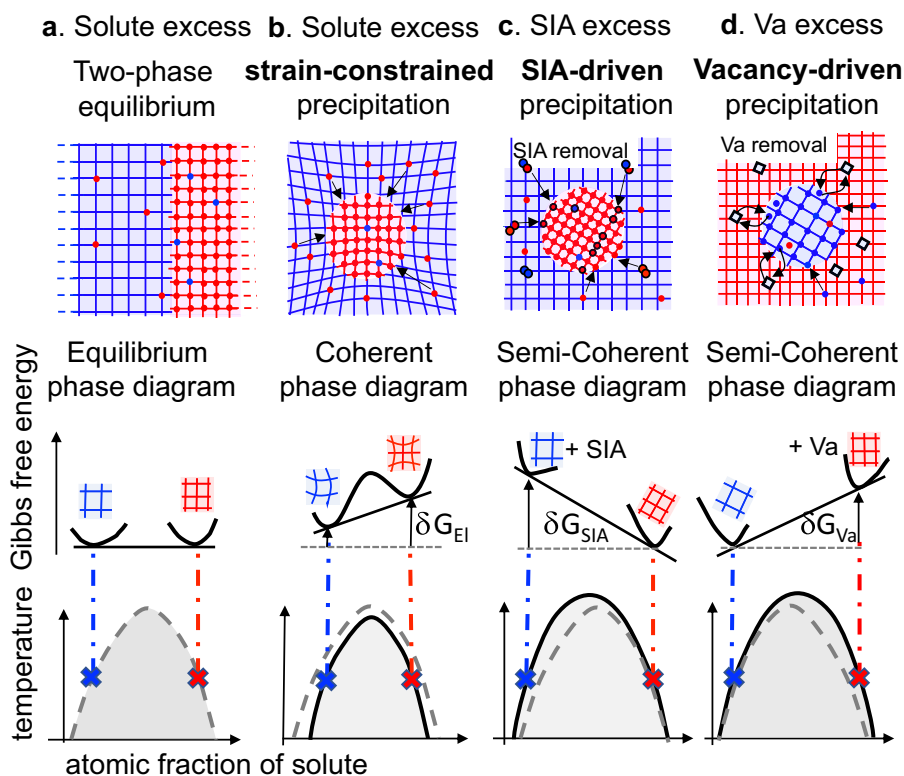


Fig. 1 Concept of semi-coherent phase diagram accounting for the point defect accommodation mechanism. Illustrations of (a) the final equilibrium state between infinite volume phases (blue and red domains), (b) a deformed precipitate (in red) in a supersaturated solution, with an elastic strain ensuring the continuity of the lattice at the precipitate/matrix interface, and reducing the two-phase domain of the phase diagram; (c, d) the semi-coherent precipitation in an undersaturated solid solution triggered by respectively an excess of self-interstitial atoms (SIA) and an excess of vacancies (Va). In (c), the precipitate eigenstrain is negative (dense precipitate). The transformation of SIAs into substitutional atoms of the precipitate increases the volume of the inclusion resulting from the phase transformation of the parent phase inclusion and decreases the excess Gibbs free energy δG_{SIA} generated by the excess of SIA. In precipitate, the extra atoms condense into finite-size atomic planes leading to misfit dislocations. In (d), the precipitate eigenstrain is positive (less dense precipitate), the exchange of Va with the atom of the precipitate reduces the volume of the transformed inclusion, and the excess Gibbs free energy δG_{Va} generated by the excess of Va. The excess of point defects enlarges the two-phase equilibrium domains so that a solid solution initially undersaturated in solute may become unstable with respect to phase separation.

of this interplay on the precipitation driving force, has been completely underestimated up to now.

Our focus is on the Fe–Ni system because it is an excellent model alloy of ferritic steels at low concentrations of Ni and of austenitic steels at a higher concentration of Ni, and its behavior under irradiation raises questions¹⁵. To investigate properly the effect of point defects, we need to produce a permanent concentration of point defects and, thus, employed an ion irradiation technique. Results presented in¹⁶ are exploited further here. Thanks to advanced thermodynamic and kinetic methods relying on DFT-based point defects properties, and atomic-scale characterization techniques, we provide direct evidence of the prominent role of point defects in phase transformations. In particular, we highlight the excess of SIAs together with the precipitate eigenstrain decreases the solubility limit of nickel in ferrite, the non-monotonous variation of the lattice parameter around the INVAR composition ($c_{\text{Ni}} \approx 35\%$)¹⁷ leads to the formation of a metastable Fe-rich austenitic phase observed both in ferrite and austenite.

Results

Experimental evidence of the role of point defects on the precipitation of austenite in ferrite. The investigated material is a bcc (body-centered cubic)-based Fe-3.3 at% Ni alloy of high purity¹⁶. The evolution of the microstructural damage upon self-ion irradiation, as a function of depth, was evaluated by high-resolution transmission electron microscopy (HRTEM) and plotted in Fig. 2¹⁶. The irradiated sample exhibits a heterogeneous microstructure attributed to the spatial radiation dose variation. Interestingly, void density increases together with precipitate density and begins to drop when the precipitate density reaches a plateau.

Microstructural characterization of one face-centered cubic (fcc) γ precipitate is presented in Fig. 3 (HRTEM images of four other precipitates are presented in Supplementary Note 1 and Fig. 1). The fast Fourier transform (FFT) of the HRTEM image, in Fig. 3f, shows a co-linearity of both the close-packed directions $[1, \bar{1}, 0]_{\text{M}}$ and $[1, \bar{1}, 1]_{\text{fcc}}$, indicating this plane remained invariant (not rotated) upon the phase transformation. The invariant-plane crystallographic model was thus developed assuming Kurjumov–Sachs orientation relationship between fcc precipitates and the bcc matrix^{1,18}. It reproduces the experimental FFT within 1% in length and within 7% in angle for the close-packed direction vectors (see colored circles superimposed on diffraction spots in Fig. 3f and Supplementary Note 2 and Table 1 for more details). We deduce, from the invariant planes' reflections, the

fcc/bcc ratio of the crystal lattice parameters: $\chi \equiv 1.247$. The latter is in very good agreement with the X-ray lattice ratio determined in macroscopic phases, spanning from $\chi = 1.249$ at 20 at% of Ni, to $\chi = 1.246$ at 50 at% of Ni in phase γ at $T = 400^\circ\text{C}$ ^{17,19}. Hence, the elastic strain of the two-phase lattice is negligible. Fig. 3 also shows that twin-related Kurjumov–Sachs crystallographic variants formed to share a mirror symmetry that coincides with the $(1, \bar{1}, 0)_{\text{M}}$ twin-boundary plane. Figure 3c displays the experimental inverse FFT (iFFT) obtained from $(1, 0, \bar{1})_{\text{M}}$, $(0, 0, 2)_{\text{V1}}$ and $(1, \bar{1}, \bar{1})_{\text{V2}}$ reflections, where Moiré fringes' width and misfit dislocations' periodicity along with the interfaces (in red) can be easily inferred. Misfit dislocations can also be seen on the direct HRTEM images (Fig. 3b). The crystallographic model assumes a perfect fcc lattice within both variants of the precipitate. Consequently, the good agreement between this model and the HRTEM observations on both iFFT and the misfit dislocation periodicity tends to prove that the eigenstrain has been compensated by the creation of fcc lattice sites in the precipitate. Based on our crystallographic model, we estimate the atomic fraction of these extra sites v_1 (cf Eq. (1) of the “Methods”). For a Ni content of γ around 30 at%, v_1 is equal to $v_1 = 1.5\%$.

As the dislocation line density is very low ($<10^8\text{ cm}^{-2}$) and dislocation loops absent in the precipitate region (Fig. 2a), dislocations are unlikely involved in the mechanism of coherency loss³, at least when precipitates grow. These extra sites might result from the transformation of SIAs of the host matrix into substitutional atoms of precipitates. A scheme of this mechanism is given in Fig. 1c, where one SIA attached to a single lattice site of the parent phase is transformed into two atoms seating on two perfect lattice sites of the precipitate when transferred. Besides, voids coexist with precipitates¹⁶. Their growth with radiation dose proves that they absorb more vacancies than SIAs. The mass balance implies precipitates absorb SIAs.

Dislocation loops take a part in the nucleation process of precipitates. Indeed, in the lower dose region, ($<1\text{ dpa}$), there are dislocation loops and no precipitates. Radiation-induced segregation²⁰ takes place through point defect and solute flux coupling²¹, leading to solute enrichment on dislocation loops. They contain up to 17 at% Ni¹⁶. By acting as local reservoirs of strain, lattice sites, and Ni atoms, Ni-decorated loops likely facilitate γ phase nucleation, similarly to what occurs in a complexion-mediated martensitic phase transformation²².

Misfit dislocations certainly control the shape of precipitates. If we assume that interface energies are proportional to the number of misfit dislocations, we may elucidate their shape by relying on a 2D-Wulff construction (Fig. 3e). $(\bar{1}\bar{2}\bar{1})_{\text{M}}$ planes (in green) are

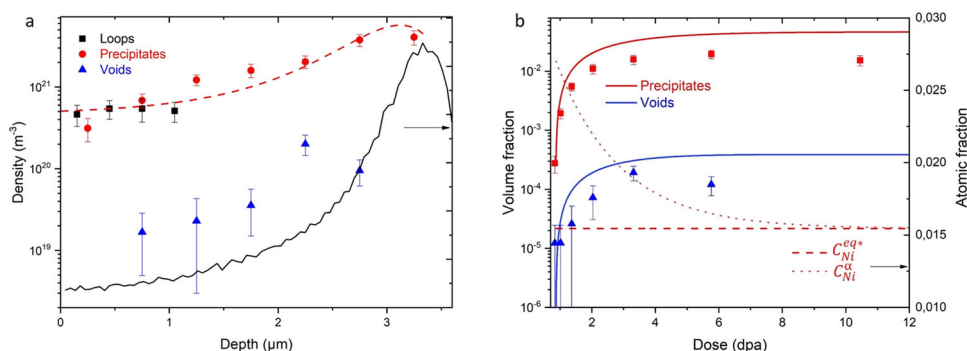


Fig. 2 Evolution of Ni content and microstructure in the function of radiation depth and dose in Fe-3.3 at% Ni. **a** Experimental densities of dislocation loops (full squares), precipitates (full circles), and voids (full triangles) with SD error bars, vs. depth at $T = 400^\circ\text{C}$. **b** The nonhomogeneous microstructure is related to the spatial variation of the radiation dose by means of the SRIM and TRIM code computing the radiation damage in terms of displacement per atom (dpa). The volume fraction of precipitates and voids, and the Ni content of the matrix α , c_{Ni}^{α} (dotted line), as measured (symbols with SD error bars) and predicted by the model (lines). The Ni content in the matrix α , converges to the metastable equilibrium atomic fraction of Ni $c_{\text{Ni}}^{\text{eq}*}$ (dashed line).

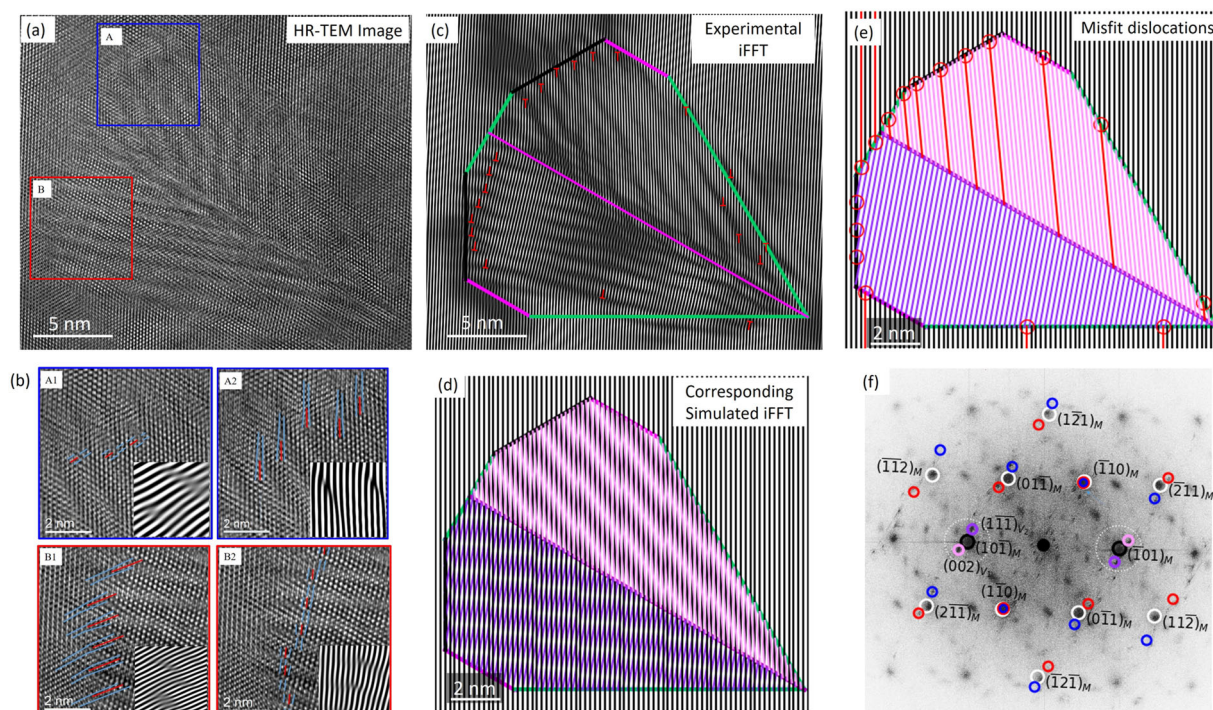


Fig. 3 The demonstration that additional lattice sites are created within semi-coherent precipitates of irradiated Fe-Ni. **a** HRTEM image of the fcc variants formed under irradiation at 400 °C at a flux of $9.6 \cdot 10^{-6}$ dpa s^{-1} within the Fe-3.3% Ni bcc matrix. fcc variants and bcc matrix are respectively in $[110]$ and $[111]$ zone axis. The schematic shape of the precipitate is superimposed. Interfaces with the invariant plane orientation, $(\bar{1}10)_M$, are in violet, $(112)_M$ and $(110)_M$ orientated interfaces are respectively in green and black. **b** Enlargement of two series of dislocation misfits between (A1) the $(01\bar{1})_M$ matrix planes and the $(111)_{V1}$ planes of variant 1 (half top of the precipitate); (A2) the $(10\bar{1})_M$ matrix planes and the $(002)_{V1}$ planes of variant 1 (half top of the precipitate); (B1) the $(01\bar{1})_M$ matrix planes and the $(00\bar{2})_{V2}$ planes of variant 2 (half bottom of the precipitate); (B2) the $(10\bar{1})_M$ matrix planes and the $(11\bar{1})_{V2}$ planes of variant 2 (half bottom of the precipitate). **c** Inverse Fast Fourier Transform (iFFT) of the $(10\bar{1})_M$ matrix planes and $(002)_{V1}$ planes of variant 1 (half top of the precipitate in pink) and the $(11\bar{1})_{V2}$ planes of variant 2 (half bottom of the precipitate in violet). **d, e** Simulated iFFT corresponding to the image (**c**). The representation of $(10\bar{1})_M$ matrix planes, $(002)_{V1}$ precipitates planes of variant 1 and $(11\bar{1})_{V2}$ precipitate planes of variant 2 in black, pink, and violet, highlight the atomic plane discontinuities, which may lead to the formation of dislocation misfits at interfaces (the extra planes are indicated as red lines and discontinuities at interfaces as red open circles). The superposition of the same matrix and precipitate planes yields Moire fringes, whose periodicity along an interface corresponds to the dislocation misfit periodicity. **f** Superposition of the experimental and simulated FFT of both the matrix and the precipitate. The Wulff-radius of interface normalized by the $(\bar{1}10)_M$ interface radius is equal to: $E_{1\bar{2}1} = E_{211} = 0.6$, and $E_{11\bar{2}} = E_{01\bar{1}} = E_{10\bar{1}} = 1.5$.

favoured against $(\bar{1}10)_M$ (in magenta) and $(01\bar{1})_M$ planes (in black): their interface energy, normalized by the $(\bar{1}10)_M$ one, are $E_{1\bar{2}1} = E_{211} = 0.7$ and $E_{01\bar{1}} = 1.6$. These ratios are very close to the experimental ones (Fig. 3c). In particular, the low energy of the $(\bar{2}11)_M$ and $(\bar{1}2\bar{1})_M$ interface planes might be at the origin of their large contribution to the precipitate/matrix interface, leading to the strongly peaked shape of the precipitates along the $[\bar{1}12]_M$ direction.

Twelve proxygrams obtained from atom probe tomography (APT) volumes, among which two are represented in Fig. 4, reveal two Ni-rich γ precipitates (≈ 45 at% Ni), together with ten Ni-poor γ precipitates (≈ 29 at% Ni). According to the equilibrium phase diagram in Fig. 5a, at the irradiation temperature of $T = 400$ °C, the alloy is undersaturated and should not decompose, and the γ phase, which would thermally precipitate in a super-saturated phase α has a Ni content of around 47 at%²³. The average Ni composition of the matrix close to the precipitate/matrix interface is 1.55 ± 0.6 at%, which is far below the thermal equilibrium solubility limit of 9 at% Ni²³, whereas the interface composition should be close to the solubility limit^{2,24}. In parallel, a Fe-1 at% Ni alloy submitted to the same irradiation conditions shows no phase decomposition. Hence, we expect the metastable solubility limit of Ni to be ≈ 1.5 at%.

Fe-Ni phase diagram under an excess of self-interstitials. As mentioned previously, when lattice deformation is not sufficient to compensate for the eigenstrain, removal or creation of lattice sites operates. This mechanism can be achieved by point defect reactions between the parent and the precipitating phases. If point defects are in excess, their chemical potentials are non-zero and fixed by external forces. Removing point defects through an accommodation mechanism of precipitation strongly reduces the overall free energy, hence increases the precipitation driving force. When initially there is no excess of point defects, the driving force of a thermal phase decomposition mediated by the production of point defects is reduced, similarly to what occurs in elastic-constrained coherent precipitation^{1,2}. A point defect-mediated precipitation driving force is, thereby, either increased or decreased by an energetic term proportional to the point defects chemical potential multiplied by the eigenstrain (see the “Methods”). Consequently, not only are the phase boundaries modified, but a non-linear variation of either point defect chemical potential or eigenstrain with composition may cause the formation of unexpected phases.

In Fe-Ni systems, radiation-induced phase transformations in both ferrite and austenite systematically involve the precipitation of denser precipitates^{25,26}. Therefore, we assume the eigenstrain is compensated by the creation of lattice sites with an atomic

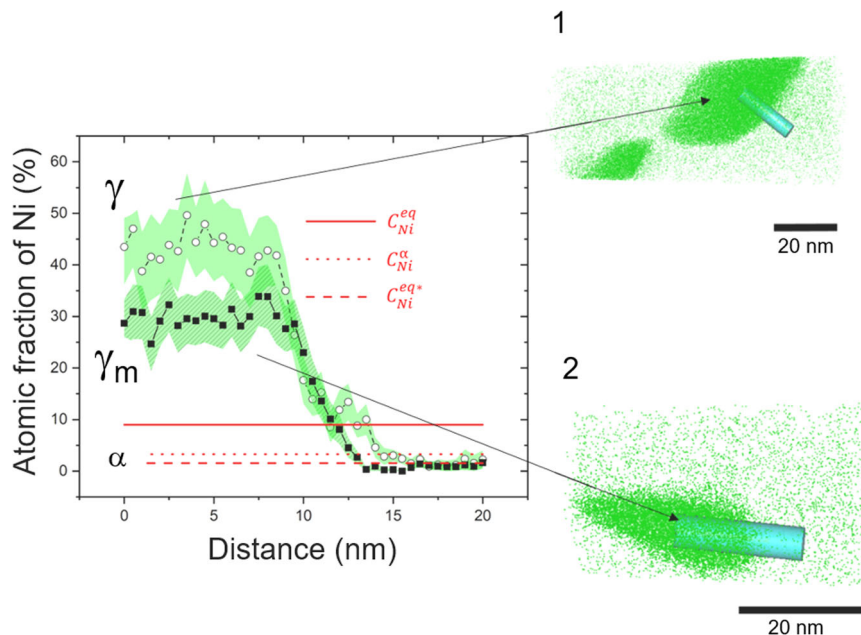


Fig. 4 Identification of a low-Ni metastable phase γ_m . APT reconstructed volumes from the Fe-3.3 at% Ni material. 1D-composition profile along with the cylinders at the interface between the α and γ phases extracted from two precipitates. Green shaded areas represent the statistical error associated with the measurement of the composition. The Ni equilibrium and metastable solubility limits, and the nominal Ni composition are respectively shown in solid, dashed, and dotted lines. Compositions of precipitates 1 and 2 are close to the ones of γ and γ_m phases respectively.

fraction of v_I , through the transformation of SIAs into substitutional atoms of the precipitating phase. As explained in “Methods”, we calculate constrained Gibbs free energies and deduce metastable phase diagrams taking into account the contribution of SIA reactions.

The most striking feature is the apparition of an austenitic Fe-rich metastable phase, γ_m , an fcc solid solution with a Ni atomic fraction roughly equal to $c_{Ni} \approx 25\text{--}30\%$ (Fig. 5). This composition is related to the atypical INVAR properties of the γ lattice parameter whose composition is plotted in Fig. 5a. At the INVAR composition, $c_{Ni} \approx 35\text{ at}\%$, the lattice parameter is maximum. When decreasing the Ni content from the position of the lattice maximum, the lattice parameter falls into a local minimum, whose position is $c_{Ni} \approx 23\text{ at}\%$ at $T = 100\text{ }^\circ\text{C}$, and slightly shifting to higher nickel content with respect to temperature. This minimum produces a local maximum of the absolute eigenstrain (or equivalently v_I in Fig. 5a). The greater the absolute eigenstrain, the greater the amount of absorbed SIAs by precipitate and the released Gibbs free energy. This produces a local minimum of the constrained free energy, leading to the formation of γ_m (Figs. 5b).

Under irradiation, whether at low and high temperature, in bcc or fcc matrix, there has been experimental evidence of this metastable phase. The precipitation of a Fe-rich γ phase was observed during ferrite-to-austenite phase transformations (ref. 16 and Fig. 4), high-temperature decomposition of γ ^{15,26}, or low-temperature $L1_0$ -ordering of austenite^{25,27}.

The ternary phase diagram of Fig. 5c calculated at $T = 400\text{ }^\circ\text{C}$, highlights the formation of two-phase equilibria involving the metastable phase γ_m : the γ_m - γ equilibrium at low concentration of SIAs, the α - γ_m and γ_m - $L1_2$ equilibria at higher supersaturation of SIAs. The supersaturation of SIAs, as well as phase thermodynamics and lattice parameters (Fig. 5a), vary with temperature. From a diffusion-reaction model of SIAs (cf “Methods” and the legend of Fig. 6), we relate the supersaturation of SIAs to the temperature and the flux of irradiation. The resulting metastable phase diagrams together with the equilibrium phase diagram are presented in Fig. 6.

In particular, Fig. 6 demonstrates that the excess of SIAs produced by irradiation induces the apparition of γ_m through the decomposition of austenite γ at high temperatures. Although our objective is not to model the kinetics of decomposition of the austenite, our continuous formulation of the constrained Gibbs free energy of phase γ (Fig. 4b) gives indications on the range of temperature and composition for which we expect a spinodal-like decomposition regime. In this regime, the variation of the composition of phases is continuous, up to their metastable equilibrium values. The spinodal limits that separate the kinetic domains between the nucleation-and-growth and the spinodal regimes are given by the zero second derivatives of the constrained Gibbs free energy²⁸. Whereas phase boundaries and the spinodal domain do not vary much around the eutectic temperature of the γ_m - γ - $L1_2$ equilibrium, the height of the miscibility gap is largely increased with the irradiation flux (Fig. 6b, d). Spinodal decomposition was observed in irradiated solid solutions at temperatures between 450 and 725 °C and nearby the INVAR composition¹⁵. This decomposition systematically features a periodic composition modulation along the [100] direction. It spans from 25 to 50% Ni with a dominant wavelength on the order of hundreds of nanometers, whatever the temperature and the incident particle (neutron, or ion). The [100] direction is the preferential direction of decomposition in cubic crystals with coherency constraints at the precipitate/matrix interface²⁹. Therefore, we expect, at an early stage of decomposition, an elastic strain partially releasing the eigenstrain, and ensuring a lattice coherency at the (100) interface (cf “Methods”). Applied to our study, simulations based on the [100] direction of decomposition effectively show that this spinodal decomposition still occurs when taking into account the coherency constraint, as reported in Fig. 6c. In this system, the elastic contribution to the Gibbs free energy is small compared to the SIA-releasing energy. Hence, adding an elastic constraint is almost equivalent to reducing the volume mismatch contribution, thereby the radiation flux, as shown by the similarities between the low flux (Fig. 6b) and high flux-coherent (Fig. 6c) phase diagrams. Ignoring the coherency constraint enlarges the two-phase domain

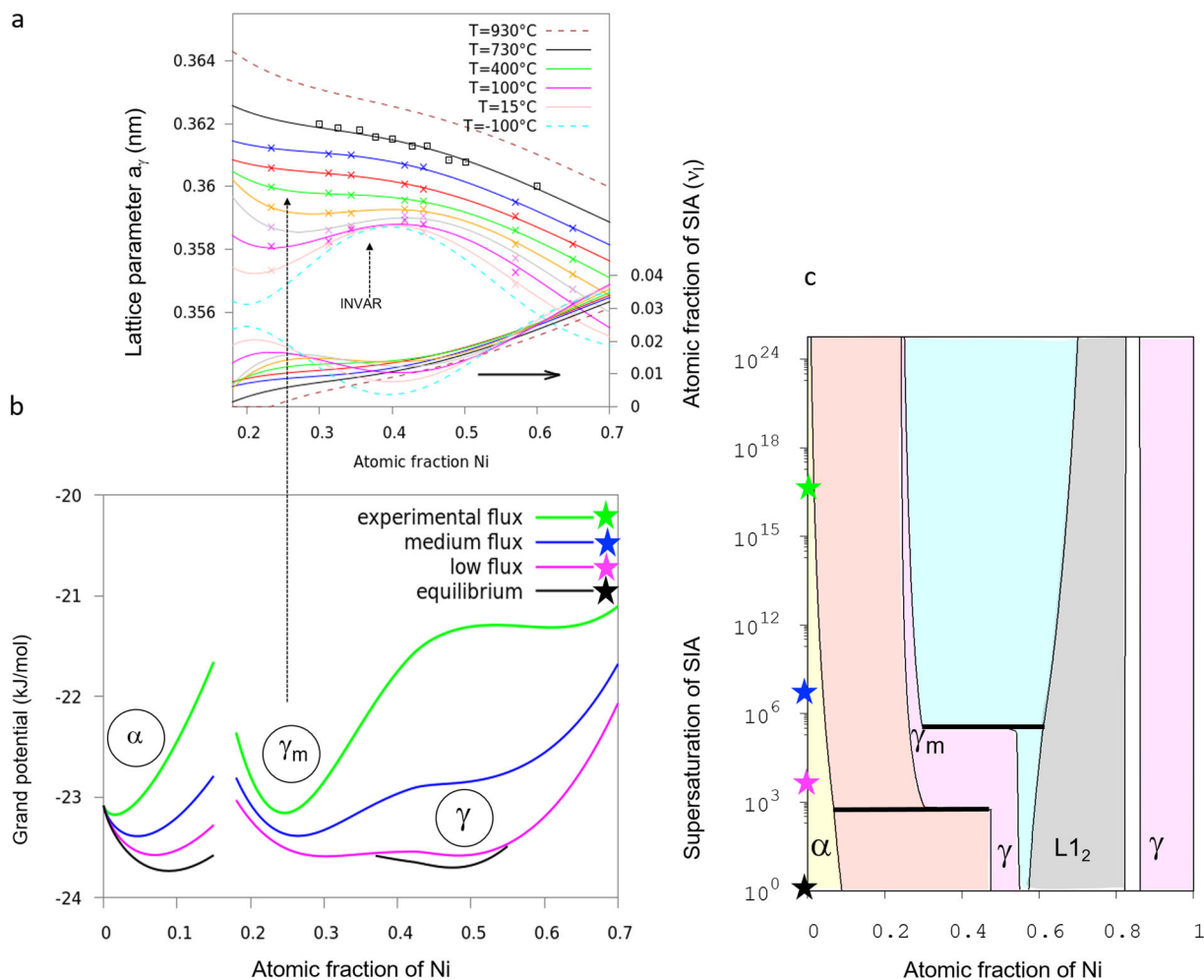


Fig. 5 The formation of the metastable phase γ_m stems from the nonlinear variation of its lattice parameter vs. Ni composition. **a** Lattice parameter a_γ of phase γ and related atomic fractions of SIAs, ν_i , deduced from a_γ and the bcc lattice parameter of phase α at $c_{\text{Ni}}^\alpha = 0.01$, with respect to the atomic fraction of Ni and temperature. Fifth order polynomial interpolation of the X-Ray experimental lattice parameter of phase γ at $T = 15, 100, 200, 300, 400, 500, 600, 730^\circ\text{C}$ (crosses are extracted from ref. 17 and squares from ref. 47). Dashed lines are obtained from a linear extrapolation of the polynomial coefficients between the two previous temperatures. Based on experimental X-ray data⁴⁸, we assume the lattice parameter of the L_{12} ordered phase is the γ one. Composition interpolation of the X-ray bcc lattice parameter⁴⁹ of phase α , a_α , is adjusted on a second-order polynomial, $a_\alpha(T = 300\text{ K}) = 0.286654 + 0.007055c_{\text{Ni}}^\alpha - 0.0359296(c_{\text{Ni}}^\alpha)^2$. Its temperature variation is deduced from an average thermal expansion coefficient¹⁹, $\alpha = 12 \times 10^{-6}\text{ K}^{-1}$. **b** Gibbs-associated grand potential with respect to the atomic fraction of Ni at $T = 400^\circ\text{C}$, at various supersaturation of SIAs, $s = c_i/c_i^{\text{eq},\alpha}$: $s = 10^{18}$ (in green, corresponding to the averaged experimental radiation flux), $s = 10^8$ (in blue), $s = 10^4$ (in magenta). The metastable phase γ_m associated with a local minimum of the grand potential comes from the local minimum of a_γ just below the INVAR composition. **c** Ternary phase diagram representing the phase boundary limits with respect to the atomic fraction of Ni and the supersaturation of SIA at $T = 400^\circ\text{C}$. Since the atomic fraction of SIAs is very small, we directly deduce the atomic fraction of Fe ($c_{\text{Fe}}^\alpha \approx 1 - c_{\text{Ni}}^\alpha$). Thick black lines indicate three-phase constrained equilibria and colored stars are the supersaturations used in panel (b).

(Fig. 6d). Therefore, we expect, at a higher dose where such coherency is lost, an increase of the separation driving force. In Fig. 6c, the minimal and maximal compositions of the measured modulation (empty blue squares) are close to the calculated lower and upper boundary limits of the γ_m - γ coherent phase domain.

Modeling of the ferrite to austenite phase transformation kinetics. As shown in Fig. 6, irradiation below $T = 700^\circ\text{C}$ largely decreases the solubility limit of Ni in the α phase. At temperatures above $T = 700^\circ\text{C}$, there is no experimental data for the γ phase. Nevertheless, an extrapolation of the fcc lattice parameter from lower temperature lattice parameters, predicts a supersaturated ferritic phase might decompose into a bcc phase α more

concentrated in Ni than the equilibrium one. This is mostly due to the high increase of the lattice parameter at low Ni content. In the undersaturated solid solution Fe-3.3 at% Ni, at $T = 400^\circ\text{C}$, irradiation caused the austenitic phase precipitation. The bulk composition in most precipitates is $\approx 29\%$, rather close to the calculated composition of the metastable γ_m phase ($\approx 23\%$ Ni). In Fig. 5b, c, at very low supersaturation of SIAs (magenta curve and star), we observe a three-phase domain including the phase α with composition $c_{\text{Ni}}^\alpha = 7\%$, the Fe-rich phase γ_m with composition $c_{\text{Ni}}^{\gamma_m} = 30\%$ and the Ni-rich phase γ with a composition very close to the equilibrium one: $c_{\text{Ni}}^\gamma = 49\%$. Consequently, in Fig. 4, the Ni-rich phase identified experimentally with composition $c_{\text{Ni}} \approx 47\%$ could be a product of this three-phase constrained equilibrium.

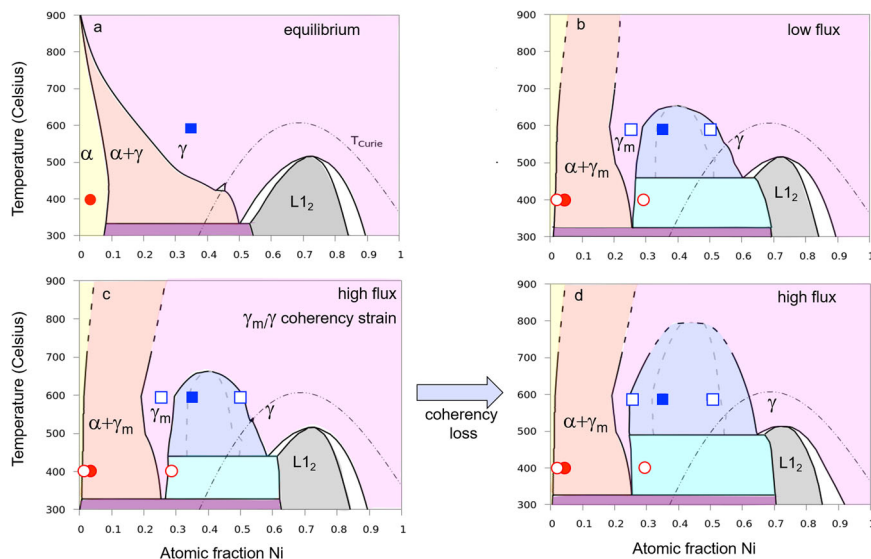


Fig. 6 Semi-coherent phase diagrams of Fe-Ni is driven by irradiation. Equilibrium (a) and radiation-induced metastable phase diagrams (b, c, d) of Fe-Ni including an SIA accommodation mechanism of the precipitate eigenstrain. In (c), part of the eigenstrain produced by the decomposition of phase γ is released by an elastic strain ensuring a coherent (100) interface. The γ_m - γ two-phase domain widens from (c) to (d), due to the release of the coherency constraint. At low and high radiation dose rates, the temperature-dependent atomic fraction of SIAs is respectively equal to $c_1 = 10^{-20} \text{ m}^2 \text{ s}^{-1}/d_i$ and $c_1 = 10^{-14} \text{ m}^2 \text{ s}^{-1}/d_i$, where c_1 and d_i are the atomic fraction and diffusion coefficient of SIAs. The product $d_i c_1$ is related to the radiation flux and the overall annihilation strength of the microstructure acting as sinks of point defects (cf the “Methods”). The dotted-dashed line and gray dashed line are respectively for the Curie temperature and the spinodal limit. In temperature domains in which there are no experimental lattice parameters, boundary limits are plotted as dashed lines. Full symbols are the nominal compositions of the precipitated and parent phases measured after irradiation. Circles are for the radiation-induced bcc-fcc phase transformation and squares are for the spinodal decomposition of austenite irradiated with neutrons⁵⁰ at 600 °C.

Ferrite decomposition does not follow a spinodal-like but rather a nucleation and growth kinetic regime, since the product fcc phase has not the same crystallographic structure as the parent one. The last step undertaken in this work aimed at retrieving numerically the growth rate of γ_m precipitates. We developed a diffusion-reaction model to compute precipitate and void volume fractions (cf “Methods”). This kinetic model relies on the constrained relationship between solute and SIA precipitation driving forces, which is mainly controlled by the number of transformed SIAs into substitutional atoms of the precipitates (equal to ν_1 multiplied by the number of precipitate lattice sites). First, regarding SIAs, as mentioned previously, the precipitation driving force according to Fig. 5a, at $T = 400$ °C (green curve), ν_1 is almost constant ($\nu_1 \approx 0.015$) between 25 and 50 at% Ni. Considering the distribution of precipitates (Fig. 2a) together with their ν_1 -dependent sink efficiency (Eq. (10)), we could determine the SIA stationary atomic fraction ($c_1^\alpha \approx 10^{-13}$ at%) and thereby, the metastable solubility limit of Ni: $c_{\text{Ni}}^{\text{eq}*} \approx 1.5$ at% (dashed red lines in Figs. 2b and 4). This value is in excellent agreement with the APT estimation of Ni composition at the matrix/precipitate interface (dotted red line in Fig. 4). Note that the increase of c_1^α with the radiation flux is too little to have an effect on $c_{\text{Ni}}^{\text{eq}*}$.

Eventually, the growth rate of precipitates mainly depends on (i) the radiation dose, (ii) the excess of Ni with respect to the metastable solubility limit, and (iii) a ratio of diffusion coefficients. The latter, according to point defect properties in Fe-Ni, comes down to the ratio of diffusion coefficients of Ni and vacancy since Ni diffusion is not mediated by SIAs at all. From a matter balance, we relate the evolution of void volume fractions to the growth of precipitates. Figure 2b reports the good agreement between the simulated (solid lines) and measured (squares and triangles) growth of precipitates and voids. From an estimation of the initial precipitate volume

fraction (1 dpa) and considering the amount of Ni atoms already distributed in precipitates at this starting observation dose, we set the initial Ni composition of ferrite to 2.7 at%. The model reproduces the rate of precipitate growth and the saturation dose at which the growth stops, though the simulated kinetics are slightly faster. This might be due to an overestimation of the vacancy concentration. Part of vacancies might be consumed to release the interface constraints, leading to a reduction of the point defect absorption bias between precipitates and voids and a slow down of the kinetics.

Discussion

In the present work, we highlight the tight relation between the point defects and atoms’ fate. This relation lasts as long as there is an excess of solute atoms in the matrix. SIAs are usually much more super-saturated than vacancies due to their higher formation energy. Thus, the precipitation of dense phases followed by the precipitation of low-density phases might occur, resembling the usual successive formation of SIA dislocation loops followed by voids in irradiated samples³⁰. Among radiation damage phenomena to be revisited, let us mention swelling³¹ and the ones naturally related to a phase transformation such as stress corrosion cracking and amorphization. The primary mechanism of swelling is the preferential elimination of SIAs at dislocations which make them climb and form new lattice sites. As long as SIAs are preferentially absorbed by dense precipitates, the creation of lattice sites does not lead to an increase of the total volume, consequently, no onset of swelling. This may explain the superior swelling resistance of bcc materials compared to fcc ones. Indeed, the open crystallographic structure of a bcc lattice widens the possibilities of hosting SIAs, that is, forming high-density precipitates. Precisely, a number of puzzling phase transformations occur in bcc nuclear materials³². Let us mention

the surprising sequence of intermetallics precipitation in both W–Re³³ and ferritic-martensitic steels^{34–37}.

Conclusions

Building semi-coherent phase diagrams and deducing kinetic laws of precipitation can now be intended using the constrained thermodynamic model developed in the present work. Our results on the Fe–Ni system demonstrate that specific partitioning of atoms and point defects between phases may move the phase boundary limits. Furthermore, it may cause the precipitation of chemical phases which do not even exist in equilibrium phase diagrams, when the variation of the phase lattice parameter or the formation energy of point defects with composition is non-monotonous.

We could produce constrained phase diagrams dedicated to successive kinetic stages of the phase transformation, an early-stage decomposition phase diagram accounting for an elastic coherency constraint along a specific lattice direction of the matrix, then a later-stage decomposition phase diagram releasing the elastic coherency constraint. Though in the present work, the thermodynamic model has been applied to semi-coherent precipitation of dense phases promoted by supersaturation of SIAs, it can be applied to the precipitation of phases less dense than the matrix promoted by supersaturation of vacancies and extended further to systems with initially no excess of point defects. Whenever semi-coherent precipitation involves a driving force well above the point defect formation enthalpy, point defects can be emitted from precipitates subsequent to a thermal phase transformation, as evidenced in semi-conductors^{38,39}. The newly point defect generated microstructure may have a dramatic impact on both functional and structural properties of materials, as for example the generation of dislocation loops leading to light-induced degradation of solar cells⁴⁰. Sources of point defects such as surfaces and dislocations, by reducing the point defect formation enthalpy and their characteristic time to reach the precipitates, could also enhance semi-coherent precipitation. We expect this mechanism to be totally relevant in nanoscale materials with precipitates systematically surrounded by surfaces⁵.

To go further, we should consider the possibility of forming non-equilibrium phases including point defects such as the ones discovered by systematic ab-initio searches of chemical phases^{37,41}. We could add more complex accommodation mechanisms involving for example the punching of dislocations loops^{3,4}.

We are only at the beginning of paving the way to incorporate kinetic constraints and accommodation mechanisms in constrained phase diagrams.

Methods

Crystallographic model. We represent the distortion of the bcc parent phase during the invariant plane strain transformation, with the matrix P_1 . P_1 is the product of a Bain strain matrix and a rotation matrix keeping the initial orientation of the $(1, \bar{1}, 0)_M$ atomic plane and the $\mathbf{A} = [1, 1, 1]_M$ direction¹. This transformation leads to the first variant of a twin-variant precipitate. The second variant has the same invariant plane and direction, but the Bain transformation is made along another axis of the cubic axis, leading to the strain transformation matrix, P_2 . Both variants share a twin-boundary and have a Kurjumov–Sachs orientation relationship with the atomic lattice of the host matrix (see Supplementary Note 2 for more details). From the calculation of the pure strain component of the strain-rotation operations leading to variants 1 and 2, we obtain the volume mismatch of the precipitate. If there is no elastic strain, it exactly corresponds to the atomic fraction of additional sites ν_1 of the precipitates

$$\nu_1 = \frac{1}{\sqrt{2}} \left(\frac{a_{fcc}}{a_{bcc}} \right)^2 + \frac{1}{\sqrt{2}} \frac{a_{fcc}}{a_{bcc}} - 2. \quad (1)$$

We compute the diffraction pattern produced by variant 1 of a precipitate by applying the matrix P_1 to the reciprocal lattice vectors of the matrix. We obtain the

Moire fringe periodicity and the density of misfit dislocations produced by a reciprocal lattice vector \mathbf{H}_{hkl}^M and its variant one $P_1 \mathbf{H}_{hkl}^M$, by computing $\mathbf{G}_{hkl}^{V1} = \mathbf{H}_{hkl}^M - P_1 \mathbf{H}_{hkl}^M$. The modulus of the inverse of \mathbf{G}_{hkl}^{V1} is equal to the Moire fringe wavelength. The projection of \mathbf{G}_{hkl}^{V1} along the interface (directed along $\mathbf{T}_{pqr}^M = \mathbf{H}_{pqr}^M \wedge \mathbf{A}$) yields an atomic plane density of misfit dislocations at the interface. If the projection is positive, the dislocations are inside precipitates, and if negative outside the precipitates. More details are given in Supplementary Note 2. We associate to every interface, a misfit dislocation density summed up over the contribution of the $(\bar{1}, 1, 0)_M$, $(\bar{1}, 0, 1)_M$ and $(0, 1, \bar{1})_M$ planes together with their respective variant planes. By assuming the semi-coherent interface energy is proportional to its corresponding misfit dislocation density, we may obtain a rough estimation of the variation of the interface energy with its orientation. In this interface energy model, note that we ignore the misfit dislocations resulting from the slight inclination of the interface plane orientation between the matrix and the precipitate.

Elastic model. We apply a standard coherency constraint on the phase decomposition of the fcc austenitic phase γ ²⁹. We impose the lattice parameters within the (100) planes to be equal between the Ni-poor phase γ_m and the Ni-rich phase γ , leading to the elastic strains, $\epsilon_{11} = \epsilon_{22} = (a_\gamma - a_{\gamma_m})/a_\gamma$. Within the isotropic approximation, the perpendicular strain along the [100] direction is equal to $\epsilon_{33} = (1 + \nu)/(1 - \nu)\epsilon_{11}$, and the elastic energy is $E_{el} = V_{tot} \Phi(1 - \Phi)(E/(1 - \nu))\epsilon_{11}^2$, where V_{tot} is the total volume of the system, Φ is the volume fraction of the secondary phase, E is the Young modulus and ν is the Poisson ratio. Note that this energy is proportional to the volume of the precipitating phase, only at first order in the volume fraction of the phase. In the case of comparable fractions of both phases, the elastic energy is a nonlinear function of the phase fractions and the level rule is invalidated. However, after numerical tests, we may neglect this effect and still represent the results after a phase diagram. We set the elastic constants to the INVAR composition values at $T = 400^\circ\text{C}$: the young modulus is set to $E = 1.6 \text{ Tdynes cm}^{-2}$ and the Poisson ratio to $\nu = 0.3$ ⁴². For the computation of the phase diagram, we subtract the elastic strain from the eigenstrain. The Poisson ratio determines the remaining eigenstrain that is accommodated by the transfer of SIA-atoms between phases. Note that the resulting phase diagram depends on the Poisson ratio only because the elastic energy is negligible with respect to the SIAs-releasing energy.

Method of calculation of semi-coherent phase diagram. As carefully demonstrated in Supplementary Note 3, we introduce a lattice-constrained chemical potential to account for the change of the lattice site number of the precipitating phase resulting from the transformation of point defects into substitutional atoms. By analogy with what is done on the thermodynamic modeling of extended defects⁴³, we assign to the atoms of the finite-size precipitate, a lattice-constrained chemical potential in addition to their atomic chemical potentials. We deduce the latter from the volume constraint on the precipitating phase and the transformation mechanism of point defects that satisfies the volume constraint. In the case of precipitates γ denser than the parent phase α and a supersaturation of SIAs, the corresponding lattice-constrained chemical potential is related to the SIA chemical potential (Supplementary Eq. (24))

$$\mu_s^\gamma = \nu_1 \mu_1^\alpha, \quad (2)$$

where ν_1 is the relative increment of the lattice site number generated in phase γ in compensation of the volume mismatch (or equivalently the volumetric eigenstrain of an inclusion α transforming into γ): $\nu_1 = -\Delta V/V$. The chemical potential of SIA, μ_1^α , is written as follows

$$\mu_1^\alpha = E_{f,1} + R_B T \ln s_1^\alpha, \quad (3)$$

where R_B is the Boltzmann constant, T the temperature, and s_1^α is the supersaturation of SIAs

$$s_1^\alpha = c_1^\alpha / c_1^{\text{eq},\alpha}. \quad (4)$$

c_1^α is the atomic fraction of SIA, and $c_1^{\text{eq},\alpha} = \exp(-E_{f,1}/(R_B T))$ is the equilibrium atomic fraction of SIA in phase α . $E_{f,1}$ is the formation enthalpy of SIA in phase α .

Note that, in the case of precipitates less dense than the parent phase and a supersaturation in vacancies, we demonstrate the lattice constrained chemical is equal to

$$\mu_s^\gamma = \nu_V \mu_V^\alpha, \quad (5)$$

where the fraction of vacancy to be absorbed is equal to $\nu_V = \Delta V/V$, and μ_V^α is the chemical potential of vacancy (see Supplementary Eq. (41)).

The conditions for thermal semi-coherent precipitation associated with the production of point defects are similar, though μ_s^γ is negative and the point defect chemical potential is set equal to its upper limit, i.e., the point defect formation enthalpy (see Supplementary Note 3, and Supplementary Eqs. (39) and (42)).

In terms of energy, a non-zero lattice-constrained chemical potential, μ_s^γ , is equivalent to adding a relaxation energy term to the Gibbs free energy of the precipitated phase γ

$$\delta G_{\text{relax}} = -N_s^\gamma \mu_s^\gamma, \quad (6)$$

where N_{γ}^{ν} is the number of lattice sites of the precipitated phase γ . We then obtain the phase boundary limits by applying the common tangent construction between this effective Gibbs free energy of phase γ and the Gibbs free energy of phase α . A common tangent construction is equivalent to subtracting from the free energies the equation of a straight line until the minima of the phases are aligned on a horizontal line. The slope of this straight line corresponds to the chemical potential and the aligned free energies are here called grand potentials (Fig. 5b).

Concentration of point defects in Fe-Ni under irradiation. Under irradiation, Frenkel pairs are created with a production rate S , the so-called radiation flux in dpa s^{-1} . Vacancies and SIAs of the Frenkel pairs may mutually recombine and annihilate at the rate R_{IV} , or diffuse to form point defects clusters such as dislocation loops and voids, or solute-SIA γ precipitates⁴⁴. Voids and precipitates when formed, become the primary point defects sinks in Fe-Ni. Far from the point defects sinks and assuming steady-state fluxes, we may write the diffusion equation of SIAs as a reaction equation

$$\frac{dc_{\text{I}}^{\alpha}}{dt} = S - R_{IV} - (k_{p,1}^2 + k_{v,1}^2)d_1c_{\text{I}}^{\alpha}, \quad (7)$$

where d_1 is the diffusion coefficient of SIA, $k_{p,1}^2$ and $k_{v,1}^2$ are respectively the sink strengths of precipitates and voids. Note that, we ignore the elimination of SIA at dislocation loops because their corresponding sink strength is very small. Although, precipitates of phase γ are not spherical, for the sake of simplicity, we rely on the spherical model of point defects sinks to write the sink strength of both the voids and the precipitates

$$k_{p,1}^2 = k_p^2 Z_{p,1}, \quad (8)$$

with

$$k_p^2 = 4\pi R_p \rho_p, \quad (9)$$

ρ_p is the volume density of precipitates and R_p is the average radius of precipitates and $Z_{p,1}$ is the sink efficiency of precipitates with respect to the SIAs. As reported in Fig. 2a, the TEM investigation (including 204 precipitates) yields a variation of the precipitate density with the distance from the surface of the sample, or equivalently with the radiation dose (varying from 0.87 to 12.26 dpa corresponding to radiation dose rates respectively equal to 5.410×10^{-6} and 7.610×10^{-5} dpa s^{-1}). We extract their volume fraction from the investigation of APT needles comprising in total 12 precipitates. By combining the APT and TEM data, we obtain an effective radius of pseudo-spherical precipitates with respect to the radiation dose rate. Both the density and the radius increase with the dose rate. After equation (8), the corresponding sink strength varies from 10^{14} to $7 \times 10^{14} \text{ m}^{-2}$, which is substantially higher than the sink strength resulting from the experimental density and average size of voids. Hence, in the following we ignore the void sink strength with respect to the precipitate one. Note that, we derive the sink efficiency after the so-called thermodynamic factor $\Phi_{\text{I,B}}^*$ (cf Supplementary Note 4 for the demonstration and Supplementary Eq. (66))

$$Z_{p,1} = 1 + \frac{\Phi_{\text{I,B}}^*(c_{\text{B}}^{\alpha} - c_{\text{B}}^{\text{eq},\alpha})}{c_{\text{B}}^{\alpha}}. \quad (10)$$

$\Phi_{\text{I,B}}^*$ is defined as the partial derivative of the matrix Gibbs free energy with respect to the atomic fractions of solute B, c_{B}^{α} , and SIA, c_{I} , in phase α (cf Supplementary Eqs. (47) and (49)). In case we may ignore the interactions between solute atoms in the matrix and assume the composition variation of precipitates is negligible, we obtain an analytical expression of the thermodynamic factor (Supplementary Eq. (57)).

$$\Phi_{\text{I,B}}^* = \frac{c_{\text{B}}^{0,\gamma} + \nu_{\text{I}}}{\nu_{\text{I}}}, \quad (11)$$

where $c_{\text{B}}^{0,\gamma}$ is the composition of the γ precipitates. When the solubility limit is reached, we have $Z_{p,1} = Z_{p,v}$, where $Z_{p,v}$ is the sink efficiency of precipitates with respect to the vacancy. Note that the latter is different from zero because the precipitate-matrix interfaces at the precipitate tips are semi-coherent and probably act as a recombination center between SIA and vacancies, maintaining a very low concentration of vacancies and SIA at the semi-coherent interface. Hence, we may write for the vacancy rate equation

$$\frac{dc_{\text{V}}^{\alpha}}{dt} = S - R_{IV} - k_p^2 Z_{p,v} d_{\text{V}} c_{\text{V}}^{\alpha}, \quad (12)$$

we assume the kinetics of SIA and vacancy are much more rapid than the solute one. Therefore, we set to zero Eqs. (7) and (12). From Eq. (7), and by assuming recombination reactions are negligible, we deduce the stationary SIA atomic fraction

$$c_{\text{I}}^{\alpha} = \frac{S}{d_1 Z_{p,1} k_p^2}, \quad (13)$$

and from the difference of Eqs. (7) and (12), the stationary atomic fraction of vacancy

$$c_{\text{V}}^{\alpha} = \frac{S}{Z_{p,v} k_p^2 d_{\text{V}}}. \quad (14)$$

For the sake of simplicity, we assume $Z_{p,v} = 1$, as if the overall precipitate interface was acting as a perfect sink for the vacancy.

Growth rate of precipitates. The rate equation associated with the matrix solute content reads

$$\frac{dc_{\text{B}}^{\alpha}}{dt} = -k_p^{0,2} \left(c_{\text{I}}^{\alpha} d_{\text{B}}^{(1)} + c_{\text{V}}^{\alpha} d_{\text{B}}^{(V)} \right) (c_{\text{B}}^{\alpha} - c_{\text{B}}^{\text{eq},\alpha}), \quad (15)$$

where $d_{\text{B}}^{(1)}$ and $d_{\text{B}}^{(V)}$ are the solute diffusion coefficients respectively mediated by SIA. Note that we ignore the effect of an SIA excess on the diffusion driving force of solutes towards precipitates because its atomic fraction never exceeds the ppm, hence its effect on the solute chemical potential is very small. We ignore as well the drag of solutes by vacancies induced by a flux coupling mechanism because the flow of solute driven by the precipitation driving force is a lot greater. Based on the assumption that every solute atom leaving the parent phase contributes to the growth of precipitates, we deduce the evolution of the precipitate volume fraction f_p

$$\frac{df_p}{dt} = -\frac{1}{c_{\text{B}}^{0,\gamma}} \frac{dc_{\text{B}}^{\alpha}}{dt}. \quad (16)$$

Since the kinetics of precipitates and voids steadily follows a matter balance, we easily relate the growth rate of voids to the growth rate of precipitates

$$\frac{df_v}{dt} = \nu_{\text{I}} \frac{df_p}{dt}. \quad (17)$$

The number of vacancies contributing to the growth of voids per time unit is equal to the number of SIAs absorbed by the precipitates per time unit.

Point defect data of Fe-Ni. The most stable configuration of SIA in Fe-Ni is a split-interstitial configuration, also called dumbbell configuration. Relying on DFT calculations of a dumbbell in pure Fe, their formation enthalpy is $E_{\text{FI}} = 3.96$ eV, their migration enthalpy is $E_{\text{m,I}} = 0.34$ eV, and the prefactor of the interstitial diffusion coefficient is d_{I}^0 to $3.3 \times 10^{-6} \text{ m}^2 \text{ s}^{-1}$ ⁴⁵. We do not account for the effect of Ni on the formation and migration energies because the interaction of the dumbbell with Ni is negligible²¹. Hence, we obtain at $T = 400$ °C, $d_{\text{I}} = 8.9 \times 10^{-9} \text{ m}^2 \text{ s}^{-1}$ and $d_{\text{Ni}}^{\text{I}} \approx 0$. We ignore the impact of Ni on the diffusion of vacancies and from a DFT diffusion database⁴⁶, we obtain at $T = 400$ °C, $d_{\text{Ni}}^{\text{V}} = 5.6 \times 10^{-12} \text{ m}^2 \text{ s}^{-1}$, and $d_{\text{V}} = 5.5 \times 10^{-12} \text{ m}^2 \text{ s}^{-1}$. Due to a strong thermodynamic and kinetic interaction between vacancies and Ni, the vacancy diffusion coefficient is very close to the Ni one.

Experimental details. The Fe-3.3 at% Ni alloy was continuously irradiated for 45 h at 400 °C at the JANNUS-Saclay facility. In total, 27 MeV Fe^{9+} ions with a flux of $8.2 \pm 2.2 \times 10^{10}$ ions $\text{cm}^{-2} \text{ s}^{-1}$ up to a fluence of $1.4 \pm 0.4 \times 10^{16}$ ions cm^{-2} were used. The damage profile was calculated with the stopping range of ions in matter (SRIM) 2008 code using Kinchin-Pease option with a displacement threshold of 40 eV. APT needles and TEM thin foils were prepared using a focused ion beam equipped on an FEI Helio 650 NanoLab dual-beam scanning electron microscopy. APT needles were taken out at a depth of 750 nm corresponding to a radiation dose rate of $7.4 \pm 1.9 \times 10^{-6}$ dpa s^{-1} and at 1200 nm with a radiation dose rate of $1 \pm 1.9 \times 10^{-5}$ dpa s^{-1} . HRTEM images were performed with a JEOL ACCEL ARM 200F Cs image corrected operating at 200 kV equipped with a Camera GATAN OneView. The APT analysis was performed using a CAMECA LEAP 4000XHR at a set-point temperature of 50 K in laser-pulsing mode at a wavelength of 382 nm, 200 kHz pulse repetition rate, and 26 pJ pulse energy. For 3D atom reconstruction, visualization, and data post-treatments, the software IVAS by CAMECA was employed. Atomic fraction profiles at interfaces were obtained with a 5 nm diameter cylinder using the algorithm 1D concentration profile with a fixed bin of 0.5 nm.

Data availability

The raw image files of Figs. 3 and 4, and the data that support the findings of this study, are available on request.

Code availability

Our code computing the phase diagram from a Calphad database and the point defect thermodynamic driving force is available on reasonable request.

Received: 17 September 2020; Accepted: 21 February 2021;

Published online: 23 March 2021

References

1. Khachaturyan, A. *Theory of Structural Transformations in Solids* (Wiley, New York, 1983).
2. Christian, J. (ed.) *The Theory of Transformations in Metals and Alloys*. <http://www.sciencedirect.com/science/article/pii/B9780080440194500374> (Pergamon, Oxford, 2002).

3. Ashby, M. F. & Johnson, L. On the generation of dislocations at misfitting particles in a ductile matrix. *Philos. Mag.* **20**, 1009–1022 (1969).
4. Brown, L. M. & Woolhouse, G. R. The loss of coherency of precipitates and the generation of dislocations. *Philos. Mag.* **21**, 329–345 (1970).
5. Bourgeois, L., Zhang, Y., Zhang, Z., Chen, Y. & Medhekar, N. V. Transforming solid-state precipitates via excess vacancies. *Nat. Commun.* **11**, 1248 (2020).
6. Kim, K., Roy, A., Gururajan, M., Wolverton, C. & Voorhees, P. First-principles/phase-field modeling of θ' precipitation in Al–Cu alloys. *Acta Mater.* **140**, 344–354 (2017).
7. Bianchini, M. et al. The interplay between thermodynamics and kinetics in the solid-state synthesis of layered oxides. *Nat. Mater.* <https://doi.org/10.1038/s41563-020-0688-6> (2020).
8. Clouet, E. et al. Complex precipitation pathways in multicomponent alloys. *Nat. Mater.* **5**, 482–488 (2006).
9. Orthacker, A. et al. Diffusion-defining atomic-scale spinodal decomposition within nanoprecipitates. *Nat. Mater.* **17**, 1101–1107 (2018).
10. Schwietert, T. K. et al. Clarifying the relationship between redox activity and electrochemical stability in solid electrolytes. *Nat. Mater.* **19**, 428–435 (2020).
11. Hong, J. et al. Metal-oxygen decoordination stabilizes anion redox in Li-rich oxides. *Nat. Mater.* **18**, 256–265 (2019).
12. Russell, K. C. The role of excess vacancies in precipitation. *Scr. Metall.* **3**, 313–316 (1969).
13. Schuler, T., Nastar, M. & Soisson, F. Vacancy-induced dissolution of precipitates in out-of-equilibrium systems: a test case of FeX (X=C, N, O) alloys. *Phys. Rev. B* **95**, 014113 (2017).
14. Marth, P. E., Aaronson, H. I., Lorimer, G. W., Bartel, T. L. & Russell, K. C. Application of heterogeneous nucleation theory to precipitate nucleation at GP zones. *Metall. Trans. A* **7**, 1519–1528 (1976).
15. Russell, K. C. & Garner, F. A. Thermal and irradiation-induced phase separation in Fe–Ni based invar-type alloys. *Metall. Trans. A* **23**, 1963–1976 (1992).
16. Belkacemi, L., Meslin, E., Décamps, B., Radiguet, B. & Henry, J. Radiation-induced bcc-fcc phase transformation in a Fe–3Ni alloy. *Acta Mater.* **161**, 61–72 (2018).
17. Owen, E. A., Yates, E. L. & Sully, A. H. An X-ray investigation of pure iron-nickel alloys. part 4: the variation of lattice-parameter with composition. *Proc. Phys. Soc.* **49**, 315–322 (1937).
18. Kurdjumow, G. & Sachs, G. Über den mechanismus der stahlhärtung. *Z. Phys.* **64**, 325–343 (1930).
19. Owen, E. A., Yates, E. L. & Sully, A. H. An x-ray investigation of pure iron-nickel alloys. part 5: the variation of thermal expansion with composition. *Proc. Phys. Soc.* **49**, 323–325 (1937).
20. Wang, X. et al. Radiation-induced segregation in a ceramic. *Nat. Mater.* <https://doi.org/10.1038/s41563-020-0683-y> (2020).
21. Messina, L., Schuler, T., Nastar, M., Marinica, M.-C. & Olsson, P. Solute diffusion by self-interstitial defects and radiation-induced segregation in ferritic Fe–X (X=Cr, Cu, Mn, Ni, P, Si) dilute alloys. *Acta Mater.* **191**, 166–185 (2020).
22. Zhang, J., Tasan, C. C., Lai, M. J., Dippel, A. C. & Raabe, D. Complexion-mediated martensitic phase transformation in Titanium. *Nat. Commun.* **8**, 14210 (2017).
23. Ohnuma, I., Shimenouchi, S., Omori, T., Ishida, K. & Kainuma, R. Experimental determination and thermodynamic evaluation of low-temperature phase equilibria in the Fe–Ni binary system. *Calphad* **67**, 101677 (2019).
24. Romig, A. D. & Goldstein, J. I. Determination of the Fe–Ni and Fe–Ni–P phase diagrams at low temperatures (700 to 300 °C). *Metall. Trans. A* **11**, 1151–1159 (1980).
25. Chamberod, A., Laugier, J. & Penisson, J. Electron irradiation effects on iron-nickel invar alloys. *J. Magn. Magn. Mater.* **10**, 139–144 (1979).
26. Garner, F., McCarthy, J., Russell, K. & Hoyt, J. Spinodal-like decomposition of Fe–35Ni and Fe–Cr–35Ni alloys during irradiation or thermal aging. *J. Nucl. Mater.* **205**, 411–425 (1993).
27. Reuter, K. B., Williams, D. B. & Goldstein, J. I. Ordering in the Fe–Ni system under electron irradiation. *Metall. Trans. A* **20**, 711–718 (1989).
28. Cahn, J. W. & Hilliard, J. E. Free energy of a nonuniform system. I. Interfacial free energy. *J. Chem. Phys.* **28**, 258–267 (1958).
29. Cahn, J. W. On spinodal decomposition. *Acta Metall.* **9**, 795–801 (1961).
30. Wiedersich, H. On the theory of void formation during irradiation. *Radiat. Eff.* **12**, 111–125 (1972).
31. Ball, P. Ordering the void. *Nat. Mater.* **19**, 589–589 (2020).
32. Marquis, E. A. et al. Nuclear reactor materials at the atomic scale. *Mater. Today* **12**, 30–37 (2009).
33. Tanno, T., Fukuda, M., Nogami, S. & Hasegawa, A. Microstructure development in neutron irradiated tungsten alloys. *Mater. Trans.* **52**, 1447–1451 (2011).
34. Hyde, J. M. et al. A comparison of the structure of solute clusters formed during thermal ageing and irradiation. *Ultramicroscopy* **111**, 664–671 (2011).
35. Wells, P. B. et al. Evolution of manganese-nickel-silicon-dominated phases in highly irradiated reactor pressure vessel steels. *Acta Mater.* **80**, 205–219 (2014).
36. Sprouster, D. et al. Structural characterization of nanoscale intermetallic precipitates in highly neutron irradiated reactor pressure vessel steels. *Scr. Mater.* **113**, 18–22 (2016).
37. Delandar, A. H., Gorbatov, O., Selleby, M., Gornostyrev, Y. & Korzhavyi, P. Ab-initio based search for late blooming phase compositions in iron alloys. *J. Nucl. Mater.* **509**, 225–236 (2018).
38. Hu, S. Nonequilibrium point defects and diffusion in silicon. *Mater. Sci. Eng.* **13**, 105–192 (1994).
39. Martin, T. P., Aldridge, H. L., Jones, K. S. & Camillo-Castillo, R. A. Use of a buried loop layer as a detector of interstitial flux during oxidation of SiGe heterostructures. *J. Vac. Sci. Technol. A* **35**, 021101 (2017).
40. Krauss, K., Fertig, F., Menzel, D. & Rein, S. Light-induced degradation of silicon solar cells with aluminiumoxide passivated rear side. *Energy Proc.* **77**, 599–606 (2015).
41. Wróbel, J. S., Nguyen-Manh, D., Kurzydowski, K. J. & Dudarev, S. L. A first-principles model for anomalous segregation in dilute ternary tungsten-rhenium-vacancy alloys. *J. Phys.* **29**, 145403 (2017).
42. Tanji, Y., Shirakawa, Y. & Moriya, H. Young's modulus, Schear modulus and compressibility of Fe–Ni(fcc) alloys. *J. Jpn. Inst. Met.* **34**, 417 (1970).
43. Liu, Z.-K. Computational thermodynamics and its applications. *Acta Mater.* **200**, 745–792 (2020).
44. Nichols, F. On the estimation of sink-absorption terms in reaction-rate-theory analysis of radiation damage. *J. Nucl. Mater.* **75**, 32–41 (1978).
45. Senninger, O. et al. Modeling radiation induced segregation in iron-chromium alloys. *Acta Mater.* **103**, 1–11 (2016).
46. Messina, L., Nastar, M., Sandberg, N. & Olsson, P. Systematic electronic-structure investigation of substitutional impurity diffusion and flux coupling in bcc iron. *Phys. Rev. B* **93**, 184302 (2016).
47. Hayase et al. Spontaneous volume magnetostriction and lattice constant of face-centered cubic Fe–Ni and Ni–Cu alloys. *J. Phys. Soc. Jpn.* **34**, 925–933 (1973).
48. Wakelin, R. J. & Yates, E. L. A study of the order-disorder transformation in iron-nickel alloys in the region FeNi₃. *Proc. Phys. Soc. Sect. B* **66**, 221–240 (1953).
49. Swartzendruber, L. J., Itkin, V. P. & Alcock, C. B. The Fe–Ni (iron-nickel) system. *J. Phase Equilib.* **13**, 585–585 (1992).
50. Garner, F., Brager, H. & McCarthy, J. *Neutron-Induced Spinodal-Like Decomposition of Fe–Ni and Fe–Ni–Cr Alloys*. 775–787 (ASTM International: West Conshohocken, PA, 1987).

Acknowledgements

The research leading to these results has been carried out in the frame of the French National Research Agency, under the “Investissements d’avenir” program (No ANR-11-EQPX-0020), in the frame of the French Agency NEEDS (CNRS-CEA-EDF-ANDRA-AREVA-IRSN-BRGM), and in the frame of EERA Joint Program for Nuclear Materials and is partly funded by the European Commission HORIZON 2020 Framework Program under the grant agreement No. 661913 (SOTERIA) and the grant agreement No. 755269 (GEMMA). The authors thank JANNuS-Saclay for irradiation, Emmanuel Clouet, and Mihai-Cosmin Marinica for their help.

Author contributions

M.N. developed the crystallographic, thermodynamic, and kinetic models. L.T.B.-R. and E.M. conceived and performed the experiments. M.L.P. with the help of L.T.B.-R. and E.M. conducted the ion irradiation experiments. All authors jointly analyzed the results and conceived the figures. M.N. wrote the manuscript and all authors reviewed the manuscript.

Competing interests

The authors declare no competing interests.

Additional information

Supplementary information The online version contains supplementary material available at <https://doi.org/10.1038/s43246-021-00136-z>.

Correspondence and requests for materials should be addressed to M.N.

Peer review information Primary handling editors: Xiaoyan Li, John Plummer.

Reprints and permission information is available at <http://www.nature.com/reprints>

Publisher's note Springer Nature remains neutral with regard to jurisdictional claims in published maps and institutional affiliations.



Open Access This article is licensed under a Creative Commons Attribution 4.0 International License, which permits use, sharing, adaptation, distribution and reproduction in any medium or format, as long as you give appropriate credit to the original author(s) and the source, provide a link to the Creative Commons license, and indicate if changes were made. The images or other third party material in this article are included in the article's Creative Commons license, unless indicated otherwise in a credit line to the material. If material is not included in the article's Creative Commons license and your intended use is not permitted by statutory regulation or exceeds the permitted use, you will need to obtain permission directly from the copyright holder. To view a copy of this license, visit <http://creativecommons.org/licenses/by/4.0/>.

© The Author(s) 2021